Electromagnetically driven dwarf tornados in turbulent convection

Saša Kenjereš
Department of Multi-Scale Physics and J.M. Burgerscentre for Fluid Dynamics, Delft University of Technology, Prins Bernhardlaan 6, 2628 BW Delft, The Netherlands

(Received 17 July 2010; accepted 22 December 2010; published online 14 January 2011)

Motivated by the concept of interdependency of turbulent flow and electromagnetic fields inside the spiraling galaxies, we explored the possibilities of generating a localized Lorentz force that will produce a three-dimensional swirling flow in weakly conductive fluids. Multiple vortical flow patterns were generated by combining arrays of permanent magnets and electrodes with supplied dc current. This concept was numerically simulated and applied to affect natural convection flow, turbulence, and heat transfer inside a rectangular enclosure heated from below and cooled from above over a range of Rayleigh numbers ($10^4 \leq \mathrm{Ra} \leq 5 \times 10^9$). The large-eddy simulations revealed that for low- and intermediate-values of Ra, the heat transfer was increased more than five times when an electromagnetic forcing was activated. In contrast to the generally accepted view that electromagnetic forcing will suppress velocity fluctuations and will increase anisotropy of turbulence, we demonstrated that localized forcing can enhance turbulence isotropy of thermal convection compared to its neutral state. © *2011 American Institute of Physics*.
[doi:10.1063/1.3541817]

I. INTRODUCTION

One of the most beautiful examples of interaction between turbulent flow and electromagnetic fields can be found inside whirlpool galaxies. Astrophysical observations and satellite measurements have confirmed a link between the spiraling pattern of the dust clouds inside such a galaxy, and the underlying magnetic field, demonstrating the origin of the magnetic fields by magnetic dynamo action.[1,2] Inspired by this example, we will explore the possibilities to apply an inverse approach—i.e., to tailor electromagnetic fields in such a way to be able to generate well-controlled three-dimensional helical flow patterns in an electrically conductive fluid. Then, we will use this concept to locally impose swirling patterns of different strengths to influence wall-heat transfer in thermally driven turbulent natural convection. The major question is to see to what extent these spiraling flow patterns (dwarf tornados) will enhance (or suppress) turbulence and wall-heat transfer in a generic turbulent natural convection situation. Also, how do these changes in wall-heat transfer compare with other forcing methods, for example, with rotation?

First, we will shortly demonstrate principles behind the generation of a single electromagnetically driven spiraling flow pattern in a closed tank filled with a weakly electrically conductive fluid. Then, we will move to a configuration with an array of permanent magnets located beneath the lower horizontal wall of the tank. For this configuration, heat transfer will be activated. Turbulent Rayleigh–Bénard convection from heated horizontal surfaces is selected as a generic situation encountered in atmospheric and oceanic flows, industrial applications such as crystal growth, cooling of electronic components, nuclear and fusion reactors, etc. Turbulence, heat transfer, and three-dimensionality are novel elements included in the present research, not previously addressed in similar studies of electromagnetically imposed flow control in shallow two-dimensional layers, e.g., Refs. 3–7.

II. EQUATIONS AND NUMERICAL METHOD

The system of equations describing turbulent flow and heat transfer for a weakly electrically conductive fluid under the presence of an external magnetic field consists of conservation of momentum, conservation of energy and divergence free conditions for the velocity (u_i), magnetic field (B_i), and total electric current (J_i), and can be written as

$$\partial_t u_i + u_j \partial_j u_i = \partial_j(\nu \partial_j u_i - \tau_{ij}) - 1/\rho \partial_i p + \sum F_i, \tag{1}$$

$$\sum F_i = F_i^B + F_i^L = \beta g_i (T_0 - T) + 1/\rho \varepsilon_{ijk} J_j B_k, \tag{2}$$

$$\partial_t T + u_j \partial_j T = \partial_j (a \partial_j T - \tau_{\theta j}), \tag{3}$$

$$\partial_i u_i = 0, \quad \partial_i B_i = 0, \quad \partial_i J_i = 0, \tag{4}$$

where ρ is the fluid density, ν the kinematic viscosity, $a = \nu/\mathrm{Pr}$ the thermal diffusivity, Pr the Prandtl number, and β the thermal expansion coefficient. Note that all variables are spatially filtered, i.e., a large-eddy simulation (LES) approach is used to be able to cover an extensive range of working parameters on a moderate numerical mesh, which is not possible using direct numerical simulations (DNSs). The sum of forces acting on the fluid consists of the thermal buoyancy force (F_i^B, modeled with the Boussinesq approximation where T_0 is the reference temperature) and the Lorentz force (F_i^L) terms. The subgrid turbulent stress τ_{ij} is modeled by a turbulent viscosity obtained from a magnetically extended Smagorinsky-type model,[8]

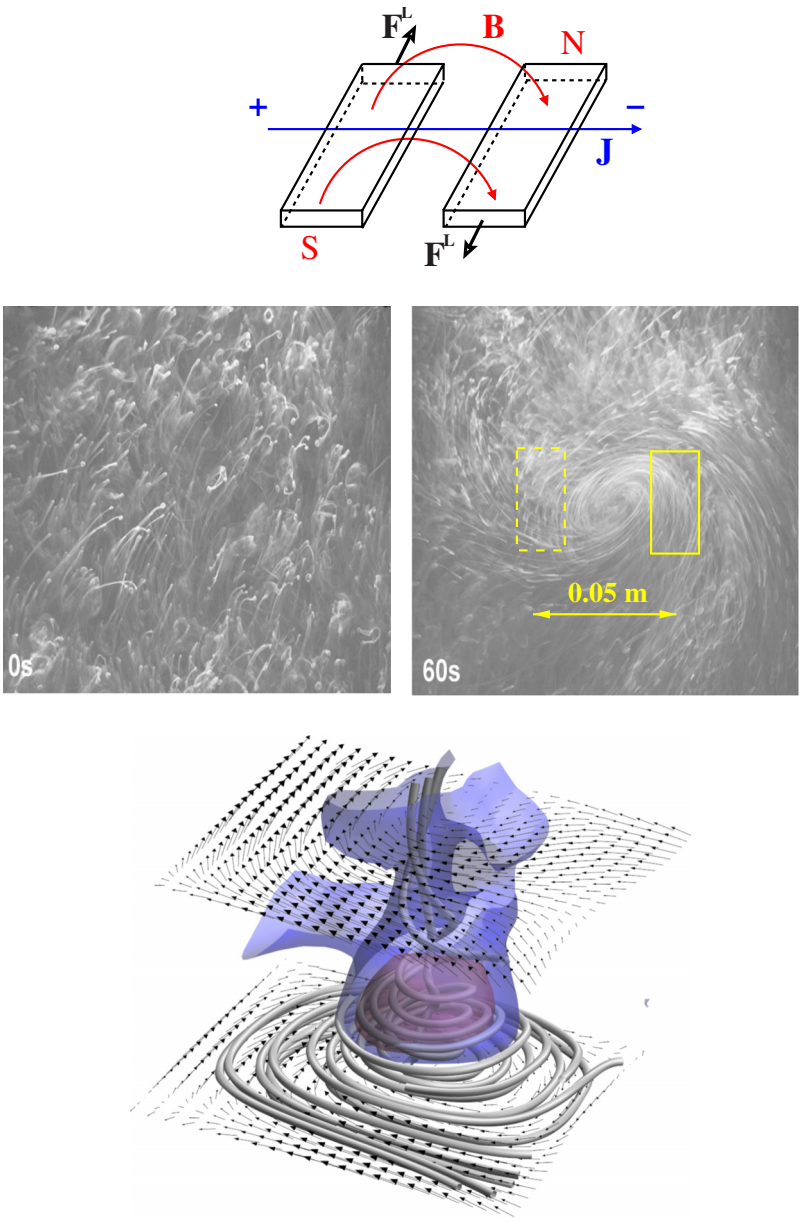

FIG. 1. (Color online) Top—schematic of the Lorentz force ($\mathbf{F^L}$) generated by two permanent magnets (S,N) and two electrodes (+,−). Middle—experimental LIF visualization of the flow generated by a configuration sketched above (no heat transfer) for two time instants (t=0 and 60 s) (Ref. 16). Bottom—visualization of the flow structures calculated by large-eddy simulation (present study): streamtraces (gray tubes), isosurfaces of the nondimensional turbulent kinetic energy $k/(|u_i|_{\max})^2$ (red=0.25, blue=0.2125) and velocity vectors in characteristic horizontal planes ($z/H=4\times10^{-3}$ and 0.5), the maximum velocity vector, $|u_i|^{2D}_{\max}=5\times10^{-3}$ m/s.

$$\tau_{ij}=\tfrac{1}{3}\tau_k k\delta_{ij}-\nu_t S_{ij},$$

$$\nu_t=\nu_s\cdot\exp\left(-\frac{\sigma}{\rho}C_m^2\Delta^2|B_0|^2/\nu_s\right),$$

$$\nu_s=C_s^2\Delta^2(S_{ij}S_{ij})^{1/2},\quad S_{ij}=\frac{1}{2}\left(\frac{\partial u_i}{\partial x_j}+\frac{\partial u_j}{\partial x_i}\right),\tag{5}$$

$$C_s=C_{s0}\left[1-\exp\left(\frac{-x_i^{N+}}{25}\right)\right]^2,\quad |B_0|=\sqrt{B_i^2}.$$

Here, the van Driest damping function is used to redefine C_{s0} in order to provide proper behavior of the turbulent viscosity in the proximity of the wall. The nondimensional wall distance from the nearest wall is given by $x_i^{N+}=x_i^N u_\tau/\nu$, where $u_\tau=\sqrt{\tau_w/\rho}$ is the friction velocity. The values of standard Smagorinsky constant and of the magnetic damping term constant are $C_{s0}=0.1$ and $C_m=1.4$, respectively, and $\Delta=(\Delta V)^{1/3}$ is the spatial filter based on the control volume. The subgrid turbulent heat flux is modeled by a simple gradient diffusion of temperature,

$$\tau_{\theta i}=-\frac{\nu_t}{\mathrm{Pr}_t}\frac{\partial T}{\partial x_i},\tag{6}$$

where $\mathrm{Pr}_t=0.86$ is the turbulent Prandtl number.

The electric (E_i) and magnetic field (B_i) distributions are calculated from a simplified set of Maxwell's equations by applying the Biot–Savart law for electrodes and permanent magnets in the form of the semianalytical solutions for three-dimensional distributions of magnetic and electric charges.[9] Note that we have a one-way coupling between magnetic fields and velocity, i.e., the initial distribution of imposed magnetic field is constant in time [the magnetic Reynolds number is very small $\mathrm{Re}_m\approx\mathcal{O}(10^{-6})$]. For our specific application, where the electric conductivity of fluid is low and generated velocity is rather moderate, Ohm's law for the to-

tal electric current density $\mathbf{J}=\sigma(\mathbf{E}+\mathbf{u}\times\mathbf{B})$ reduces to $\mathbf{J}=\sigma\mathbf{E}$, i.e., the inductive current is negligible due to $\|\mathbf{E}\|/\|\mathbf{u}\times\mathbf{B}\| > 10^3$. The identical approximation is used in studies of Rossi *et al.*,[4,5] Berger *et al.*,[10] Lardeau *et al.*,[11] and Kenjereš *et al.*,[12] and a very good agreement between performed simulations and experimental studies is obtained. This additionally confirms the validity of the used approximation. Because the imposed strengths of electric dc current and magnets are constant in time, the generated Lorentz force will also be constant in time, leading to a fully closed system of one-way [flow/electromagnetic forcing (EMF)] coupled equations. Here we will mention that the system of Eqs. (1)–(4) is discretized and solved by a second-order finite-volume solver for general (nonorthogonal) structured multiblock geometries. Additional details of the numerical method are given in Kenjereš and Hanjalić[13,14] and Kenjereš.[15]

III. RESULTS AND DISCUSSION

A. Electromagnetically driven dwarf tornado

The principle behind the generation of an electromagnetically driven dwarf tornado is demonstrated in Fig. 1. A pair of cuboidal permanent magnets (with dimensions of $0.084\times0.04\times0.04$ m^3, $|B_0|=1$ T) of different polarities is located beneath the rectangular tank (dimensions are $0.6\times0.6\times0.155$ m^3) filled with weakly conductive fluid (saltwater, $\sigma=5.5$ S/m). Also a dc current of opposite polarities (+ and −) is supplied through two electrodes perpendicular to the magnetic field lines. The electrodes are located in the upper-left and upper-right corners of the tank and extend along the entire length of the side walls. The Lorentz force, which is generated by combining the magnetic field with a dc current between two electrodes, imposes a strong planar shear that produces a swirling flow with a characteristic low-pressure region. The strength of the swirling is controlled by the intensity of the applied current. The experimental laser induced fluorescence (LIF) visualization (top view) of the flow pattern generated by this simple configuration is shown in Fig. 1—middle.[16] The flow is initially at rest (t=0 s) and by supplying dc current, a stable central vortical pattern is generated (t=60 s). Note that the single applied magnetic field is not able to generate any motion due to weak electric conductivity of the working fluid. Only the combined effects of magnets and electrodes are able to produce sufficiently strong forcing and to generate the flow motion. In contrast to experimental visualizations that are confined to characteristic planes, numerical simulations can provide full three-dimensional flow features. We present such an example in Fig. 1—bottom. Here, by plotting streamtraces of resolved velocity field a spiraling core can be easily identified. Also, isosurfaces of the turbulence kinetic energy are shown—indicating strong velocity fluctuations in the core. The velocity vectors in characteristic horizontal planes confirm existing spiraling patterns too, in good qualitative agreement with experimental observations.[12] A zoom-in of the horizontal velocity projections and streamtraces (blue lines) in characteristic horizontal planes ($z/H=0.03$ and 0.25) is shown in Fig. 2. It can be clearly seen how the strong initial shear in the lower horizontal plane ($z/H=0.03$, Fig. 2—top) leads to generation of the distinct centrally located vortical structure, Fig. 2—bottom. In addition, two smaller diagonally located spiraling patterns of weaker intensity are also created.

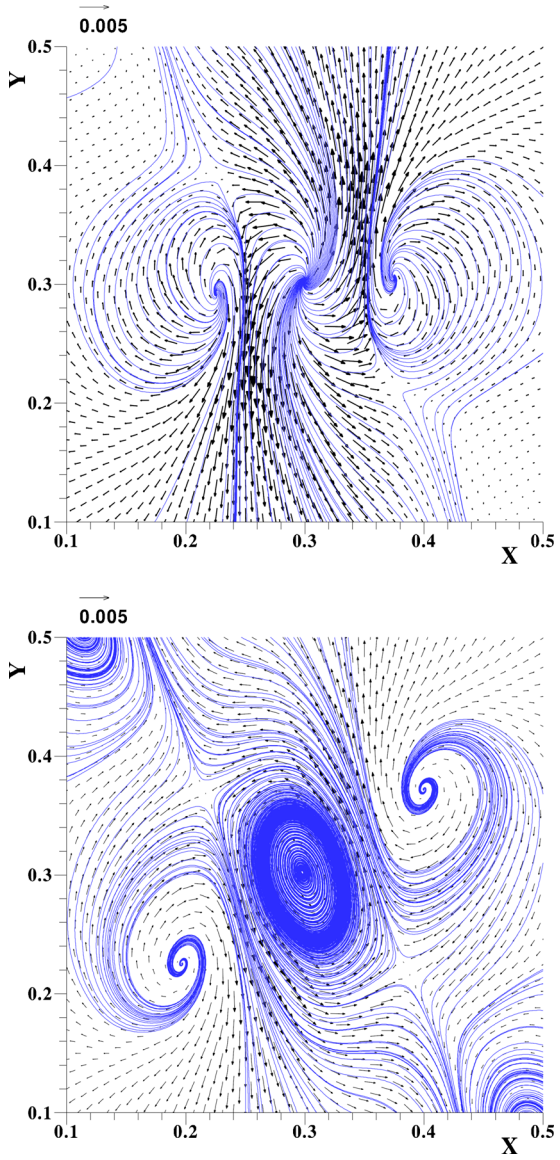

FIG. 2. (Color online) The long-term averaged resolved velocity vectors (in m/s) and streamtraces (blue lines) in two characteristic horizontal planes ($z/H=0.03$—top, $z/H=0.25$—bottom) in a fully developed state for two-magnet configuration shown in Fig. 1.

B. Multiple-dwarf tornados in turbulent convection

Similarly, by combining several magnets, multiple-vortical flow patterns can be generated. We will exploit this feature to see how such organized flow structures affect background turbulence and wall-heat transfer in turbulent Rayleigh–Bénard convection inside a finite-aspect ratio (4:4:1) enclosure with adiabatic side walls of height H and bottom-top temperature difference ΔT. We covered an extensive range of Rayleigh numbers, $10^4\leq \mathrm{Ra}\leq 5\times10^9$ ($\mathrm{Ra}=\beta g\Delta T\ \mathrm{Pr}\ H^3/\nu^2$), i.e., both soft and hard turbulence states are represented. Also, weak and strong electromagnetic forc-

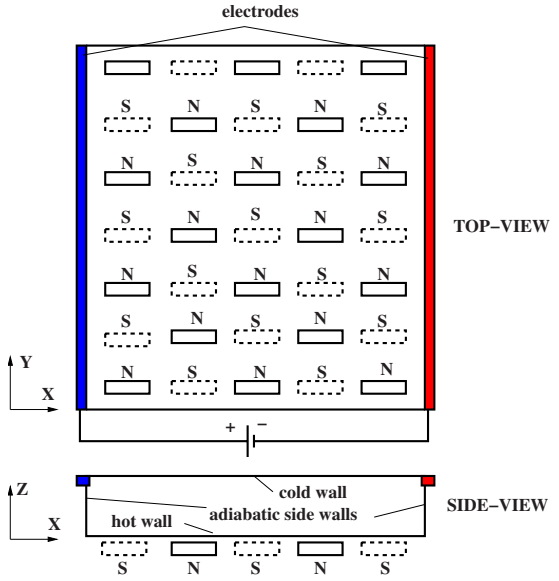

FIG. 3. (Color online) Sketch of the setup with imposed dc current through electrodes [red (right) and blue (left) sides] and permanent magnets of opposite polarities.

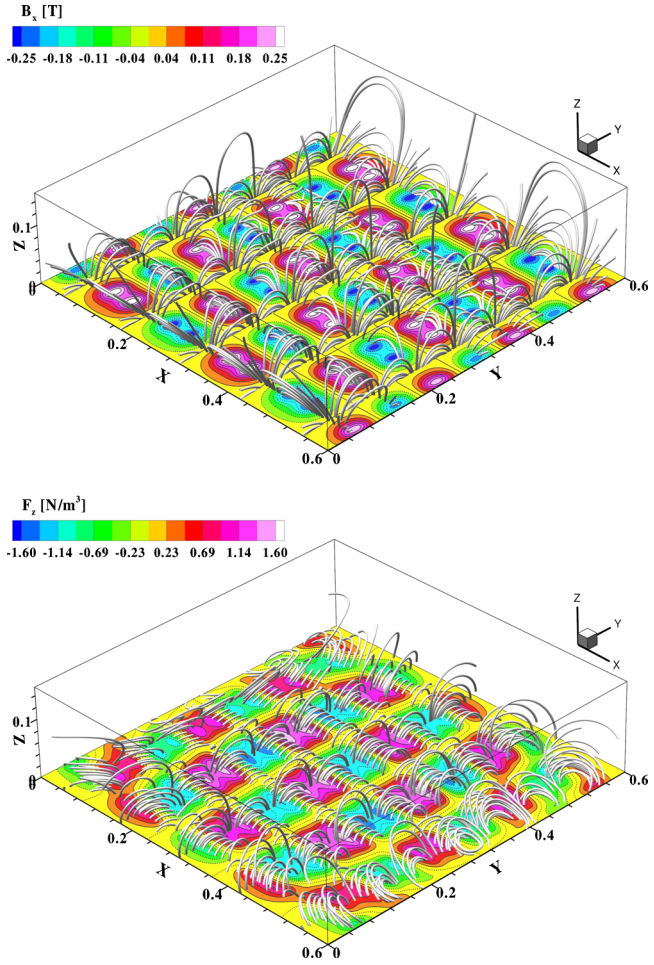

FIG. 4. (Color online) The magnetic flux lines (top) and the Lorentz force lines (bottom) are represented by gray tubes. Contours of the horizontal magnetic field (B_x in T) (top) and of the vertical Lorentz force (F_z in N/m^3) for applied dc current of I=1 A (bottom) at the lower wall of the [4:4:1] aspect ratio wall-bounded enclosure shown in the previous Fig. 3.

ing are applied, I=0,1,10 A, while the imposed magnetic fields are fixed (permanent magnets, $|B_0|=1$ T).

Direct comparisons between numerical results and particle imaging velocimetry data for an isothermal case with two- and three-magnets are reported in Kenjereš *et al.*[12] A very good agreement between measurements and LES results was obtained. This proved correct implementation of the imposed electromagnetic forcing. In addition, we also studied in details neutral turbulent thermal convection (without EMF) over a range or Rayleigh numbers, see Kenjereš and Hanjalić.[17,18] This gives credence to LES approach in dealing with wall-bounded flows subjected to the combined effects of the thermal buoyancy and imposed electromagnetic fields.

The sketch of the setup with many magnets is shown in Fig. 3—top. Dimensions of the setup and permanent magnets are identical to the setup described in Sec. III A and in Fig. 1. The dc currents of different strengths are supplied through the electrodes distributed along the vertical side walls (red and blue lines). The array of the permanent magnets is located beneath the lower heated wall. The simulation domain of this setup was presented by $182^2\times 92$ control volumes (CVs) clustered in the proximity of thermally active horizontal and adiabatic side walls. The typical averaged value of the nondimensional wall distance was $(x_w^+, z_w^+) \approx 0.5$. The clustered nonuniform mesh was designed to fully resolve the estimated flow structures in the proximity of the walls with $\Delta \approx (1-2)\eta_B$, where $\eta_B = \eta_k/\mathrm{Pr}^{1/2}$ and $\eta_k = (\nu^3/\varepsilon)^{1/4}$ are Batchelor and Kolmogorov length scales, respectively. The dissipation rate of the turbulent kinetic energy is estimated as $\varepsilon \approx |u_i|^3_{\max}/H$. The thermal boundary layers along the horizontal walls where strong temperature gradients are created were properly resolved by using 5–10 CVs in these regions. The time step was specified in order to satisfy that the maximum value of the CFL (Courant–Friedrichs–Lewy) number was 0.5. Between 5×10^4 (EMF off) and 7.5×10^4 (EMF on) instantaneous fields are used to calculate the long-term averaged fields.

The imprints of the horizontal magnetic field and of the vertical Lorentz force at the lower wall, together with three-dimensional magnetic-flux lines and Lorentz force lines distributions, are shown in Fig. 4. The strong magnetic field is primarily located in the proximity of the lower wall and it decreases with the vertical distance. This also defines the localized influence of the Lorentz force that is confined to the lower part of the simulated domain. Due to the negligible value of the induced current, this electromagnetic forcing stays constant both in time and space. The profiles of the magnetic field and Lorentz force components in the central vertical plane ($y=0.3$ m) for different distances from the horizontal wall are shown in Fig. 5. It can be seen that above the enclosure middle-height ($z=0.075$ m), the direct influence of the imposed electromagnetic forcing is small.

Now we move to the analysis of the flow and turbulence patterns generated by such imposed electromagnetic forcing. In order to be able to identify changes caused by this localized forcing, a neutral case (EMF off) of the fully developed turbulent background case of the thermal convection at Ra

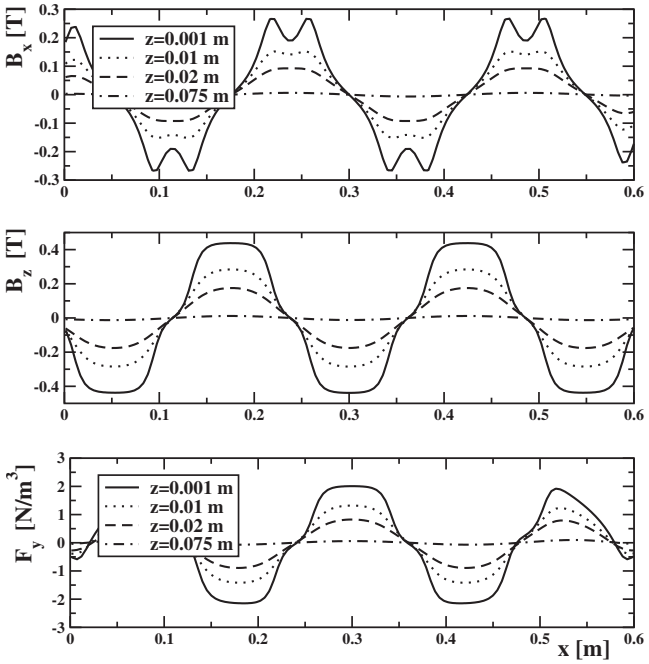

FIG. 5. Profiles of the horizontal (B_x) and vertical (B_z) magnetic field components and spanwise (F_y) component of the Lorentz force (for applied dc current of I=1 A) in the central vertical plane (y=0.3 m) for different distances from the horizontal wall.

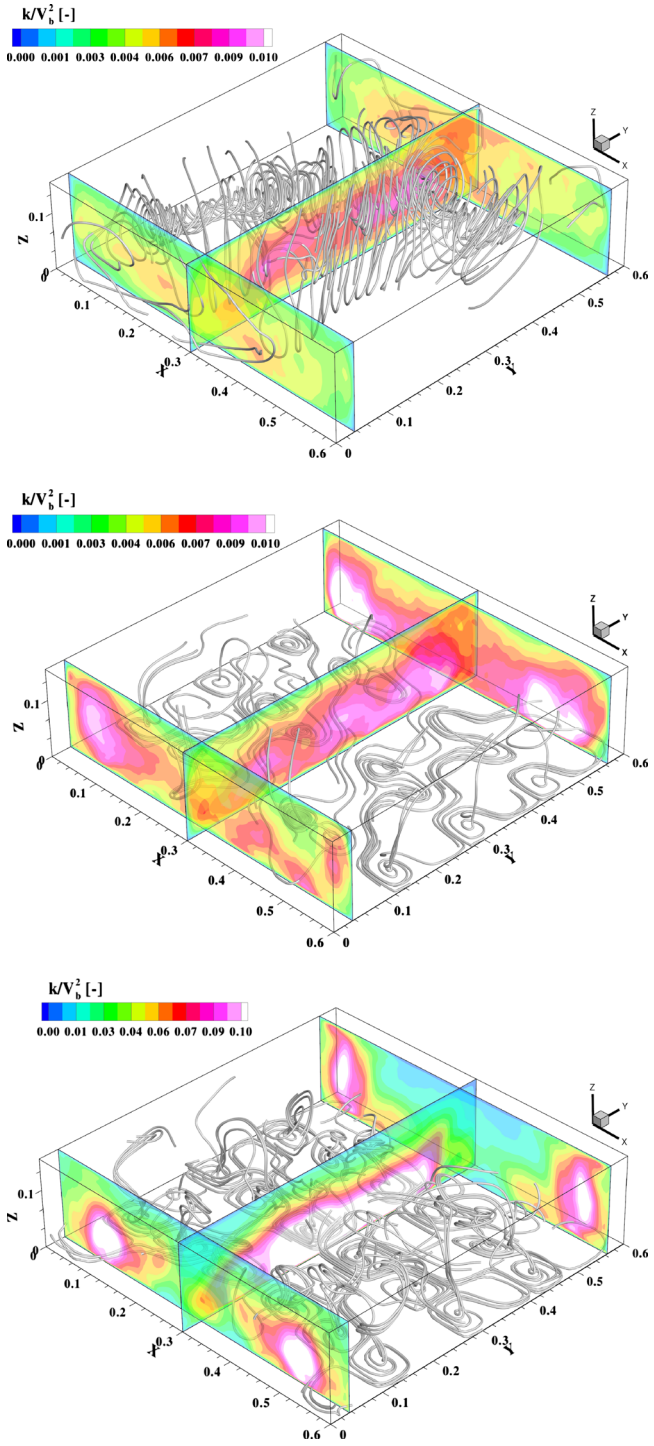

FIG. 6. (Color online) Streamtraces (gray tubes) and contours of the nondimensional turbulent kinetic energy k/V_b^2 (where $V_b=\sqrt{\beta g \Delta T H}=0.03$ m/s is the buoyancy velocity) in three characteristic vertical planes, $x/L=0.5$ and $y/D=0.1, 0.9$. The working parameters are $\mathrm{Ra}=10^8$, Pr=7, I=0 A (top), 1 A (middle), 10 A (bottom). The range of flow regimes is $500 \le \mathrm{Re} \le 8\times 10^3$ for $0 \le \mathrm{I} \le 10$ A, where $\mathrm{Re}=|u_i|_{\max} H/\nu$.

$=10^8$, Pr=7 is simulated first, Fig. 6—top. The streamtraces of the long-term averaged resolved velocity field show characteristic large-eddy structures (convective cells) of different orientations and size. The contours of the resolved turbulence kinetic energy (nondimensionalized by characteristic buoyancy velocity, $V_b=\sqrt{\beta g \Delta T H}$) in characteristic vertical planes reveal the highly turbulent core in the enclosure center. By switching on dc current of I=1 A through electrodes, a flow reorganization takes place, Fig. 6—middle. The streamtraces are now more vertically oriented and some distinct spiraling imprints are visible in the near-wall region. The turbulence kinetic energy contours depict enhanced mixing regions for all characteristic planes—although the magnitude is just slightly increased. Finally, for I=10 A, the distinct three-dimensional spiraling structures are clearly visible, Fig. 6—bottom. The distributions of turbulence kinetic energy clearly show significant asymmetry in the vertical direction. The regions with highest turbulence are located in the lower part of the enclosure. The velocity vectors and contours of the turbulence kinetic energy in two characteristic horizontal planes and for different intensity of applied forcing (I=0, 1, and 10 A) are shown in Fig. 7. The left column is for a plane in the proximity of the lower thermally active wall ($z/H=0.016$) and the right column is for the central horizontal plane ($z/H=0.5$). For the neutral case, a diagonal flow organization is observed. In the proximity of the lower wall, velocity vectors indicate an absence of vortical structures in boundary layers, Fig. 7—top left. In contrast to that, the vortical structures are clearly visible in the central horizontal plane, Fig. 7—top right. The weak EMF already imposes significant changes inside the boundary layer—where vortical structures are already present, Fig. 7—middle left. For this forcing, the vortical structures are moved toward the side walls and some traces of weak vortical structures are represented in the enclosure central part, Fig. 7—middle right. Finally, for the strongest forcing, flow is completely symmetrical with respect to the central hori-

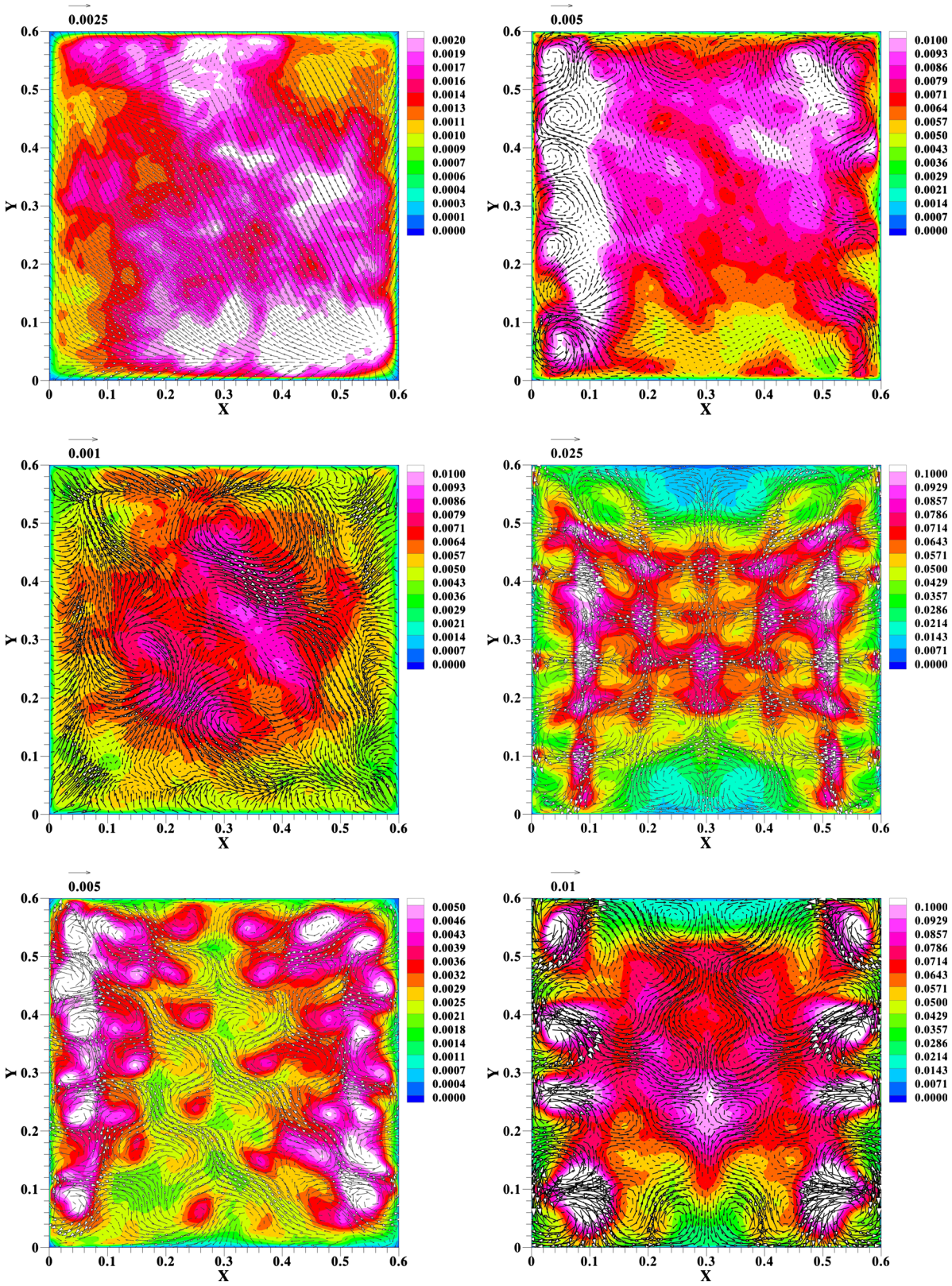

FIG. 7. (Color online) Contours of the nondimensional resolved turbulence kinetic energy (k/V_b^2) and velocity vectors (in m/s) in two characteristic horizontal planes: in the proximity of the lower wall ($z/H=0.016$—left) and in the enclosure centerplane ($z/H=0.5$—right) for Ra$=10^8$, Pr$=7$.

zontal symmetry line ($x=0.3$ m), Fig. 7—bottom. The magnitude of the velocity and of turbulence kinetic energy is significantly increased too.

The long-time averaged resolved velocity and turbulence kinetic energy in the central vertical plane ($y=0.3$ m) are shown in Fig. 8. The mean flow velocity field shows a remarkable agreement with experimental studies of Verdoold *et al.*[19] for the neutral case, Fig. 8—top. The two corotating

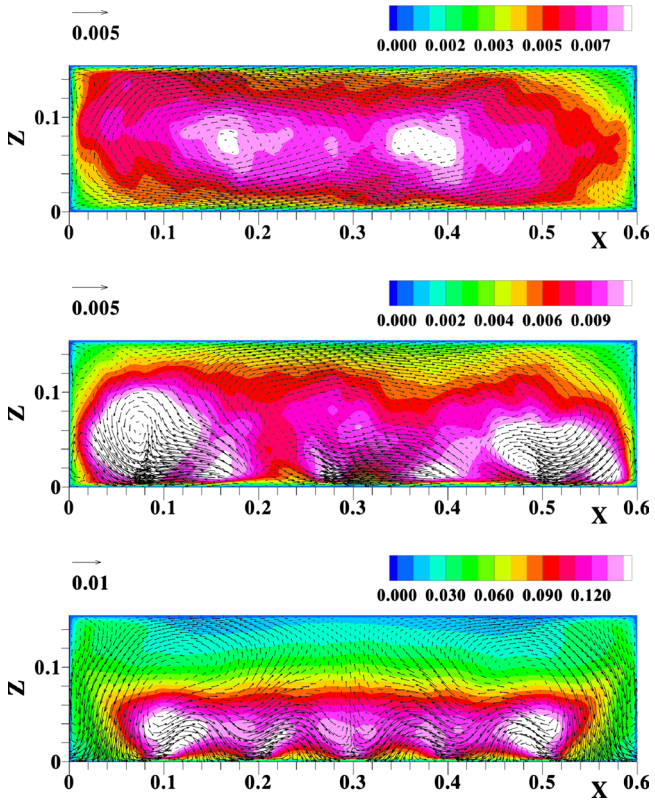

FIG. 8. (Color online) The long-time averaged resolved velocity (in m/s) and turbulence kinetic energy (k/V_b^2) in the central vertical plane ($y=0.3$ m) for Ra$=10^8$, Pr$=7$, and I$=0$ A (top), I$=1$ A (middle), I$=10$ A (bottom).

convective rolls identified in Verdoold *et al.*[19] are clearly visible. In addition, two secondary rolls located in the upper-left and lower right corners are also captured. There is also a symmetrical distribution of turbulence kinetic energy in respect to the central horizontal line. For cases with EMF, the boundary layer patterns in proximity of the lower wall are characterized by a series of consecutive vertical ejections, Fig. 8—middle and bottom. The regions of strong turbulent kinetic energy production move toward the lower wall.

The long-term averaged temperature fields are used to evaluate distributions of the thermal buoyancy force shown in Fig. 9. Note that in contrast to the electromagnetic force, this force varies both in time and space, since it depends from the underlying resolved temperature field. In the proximity of the lower thermally active wall ($z=0.001$ m), it shows significant variations in the horizontal direction due to spatial reorganization of the thermal boundary layer. To portray the redistribution of the energy among the fluctuating velocity components, vertical profiles of the turbulent stresses, for neutral and EMF case, are shown in Fig. 10. While the neutral situation shows symmetrical distributions for all stresses with respect to the central horizontal line ($z/H=0.5$), EMF generates strongly asymmetric distributions. The horizontal turbulent stresses for the forcing case have peaks that are significantly higher ($\approx 100\%$) compared to the neutral situation, but the vertical locations of their peak values stay practically identical to the neutral case. The location of the peak of the vertical turbulent stress component moves from $z/H=0.5$ to $z/H=0.3$. To obtain detailed

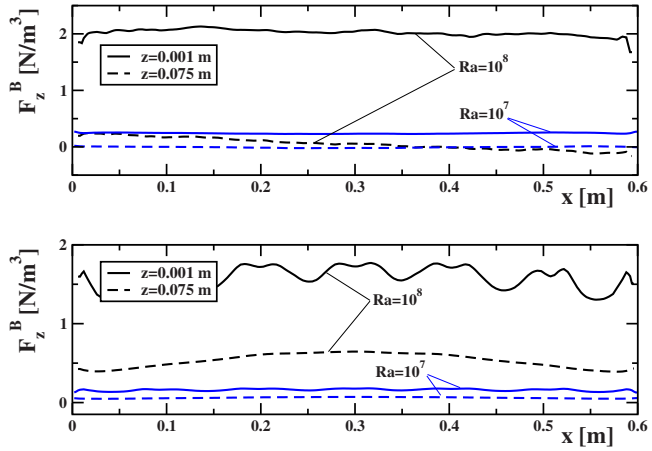

FIG. 9. (Color online) Profiles of the thermal buoyancy force (in the vertical direction) for a long-term averaged temperature field at Ra$=10^7$ and 10^8 in the central vertical plane ($y=0.3$ m) for different distances from the horizontal wall. Top—neutral case; bottom—applied dc current of I$=10$ A.

insights into turbulence anisotropy, invariants of the turbulent stresses are shown in Fig. 11. The invariants of the turbulent stress are defined as $A_2=a_{ij}a_{ji}$, $A_3=a_{ij}a_{jk}a_{ki}$, where $a_{ij}=\overline{u_iu_j}/k-2/3\delta_{ij}$ is the corresponding anisotropy tensor and $A=1-9(A_2-A_3)/8$ is Lumley's flatness parameter.[20] The latter one is a simple parameter to define deviations from the isotropic turbulence ($A=1$), and it vanishes in two-component turbulence ($A=0$).[21] Compared to the standard case of the pressure-driven channel flow, where all components of the normal turbulent stress have peak values in the proximity of the walls, for neutral turbulent thermal convection case, the vertical component ($\langle ww \rangle$) reaches its peak value exactly in the enclosure center. Also, all three components of the turbulent shear stress are important too. These specific features of the turbulent stress give negative values of A_3.

It is generally accepted that an imposed uniform magnetic field enhances turbulence anisotropy. This is observed

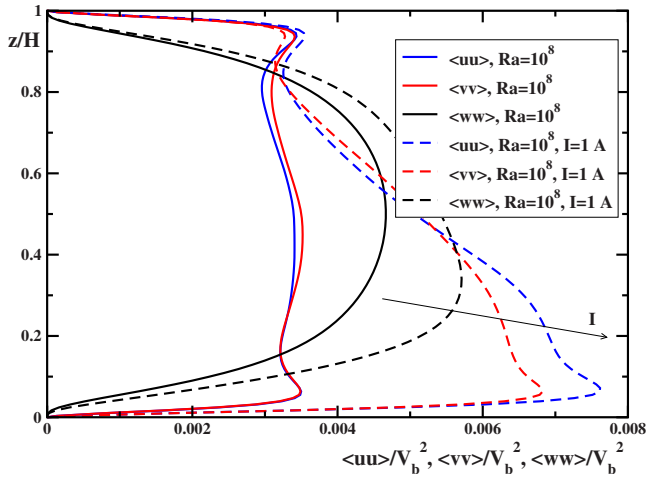

FIG. 10. (Color online) The long-time and spatially (in horizontal plane) averaged vertical profiles of the turbulent stresses without (solid lines) and with (dashed lines) imposed electromagnetic forcing (I$=1$ A), Ra$=10^8$, Pr$=7$.

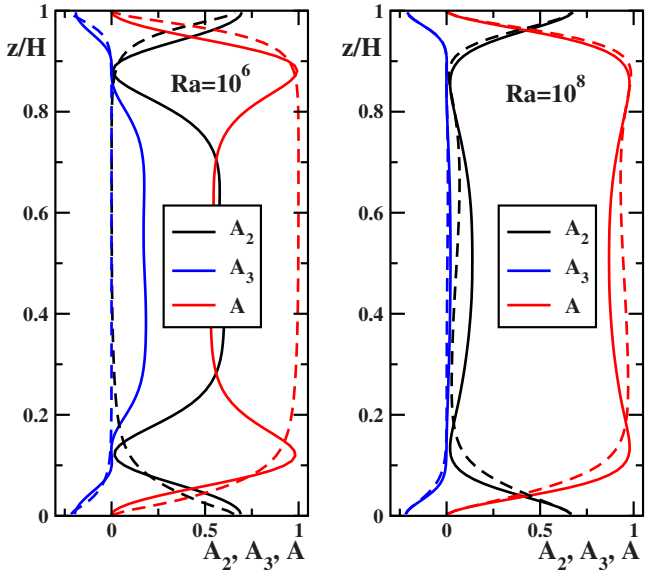

FIG. 11. (Color online) The vertical profiles of the second (A_2) and third (A_3) invariants of the turbulent stresses and flatness parameter (A) for two different values of Ra=10^6 (left) and Ra=10^8 (right) without (solid lines) and with (dashed lines) electromagnetic forcing (I=1 A).

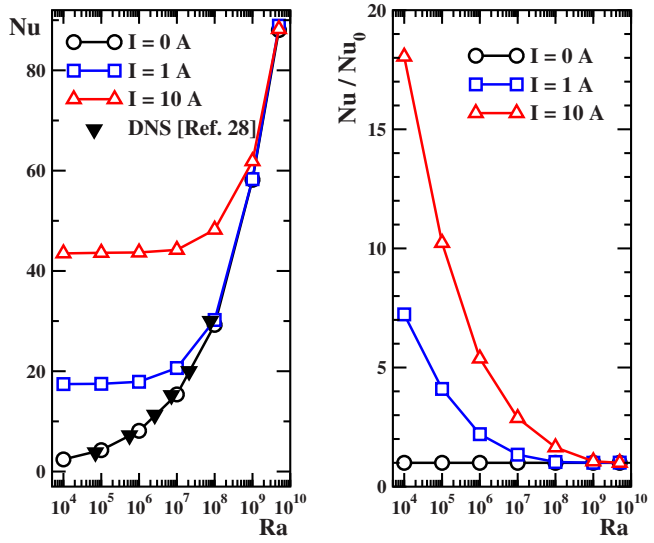

FIG. 12. (Color online) Integral heat transfer coefficient (Nu=hH/a, where h is convective heat transfer coefficient) at the lower wall for different Ra =$10^4,\ldots,5\times10^9$ and different strength if the imposed dc current I =1,10 A (left). The DNSs of Ref. 28 are shown for the neutral case; heat transfer enhancement for simulated cases (right).

for an initially homogeneous turbulence subjected to an external uniformly distributed magnetic field, as reported in Alemany *et al.*[22] and Sommeria and Moreau.[23] Also, for a turbulent Rayleigh–Bénard convection subjected to an external uniform magnetic field, the turbulence anisotropy is also increased. This is experimentally confirmed in Cioni *et al.*[24] and numerically in Hanjalić and Kenjereš[25,26] and Kenjereš and Hanjalić.[27] For the configuration studied here, we observed opposite trends. Comparing the vertical distributions of the flatness parameter (A) in Fig. 11, it can be seen that the EMF actually brings the values of A closer to one in the central part of the enclosure compared to its neutral case. It indicates that the level of isotropy is significantly increased in this region for both values of Ra. The changes are more pronounced for the smaller value of Ra=10^6 where the neutral situation shows departure from the isotropic turbulence even in the central region, Fig. 11—left.

The integral heat transfer (Nusselt number, Nu) dependence over a range of Ra and for different strengths of the imposed current is shown in Fig. 12—left. The results of the neutral case are compared with the DNS data of Verdoold *et al.*[28] Despite differences in numerical discretization (finite volume versus spectral code) and in the numerical mesh used (up to $384^2\times160$ in DNS), an excellent agreement is obtained. It confirms that here the LES used is a proper method for dealing with wall-bounded flows subjected to combined effects of the thermal buoyancy and locally imposed electromagnetic fields. Special attention was devoted to properly resolve both thermal and hydrodynamical boundary layers along walls (both horizontal thermally active and remaining side walls). The major contribution of the subgrid turbulence model is in the central part of the enclosure where the applied numerical mesh was not sufficiently fine to fully resolve all flow scales. Another advantage of using LES instead of DNS was that significantly higher values of Ra—up to 5×10^9—were simulated and that a significantly larger number of instantaneous realizations can be generated to obtain reliable long-term averaged statistics. Three distinct regimes can be distinguished in Nu-Ra distributions, Fig. 12—left: the initial state that is, strongly dominated by EMF [Ra$\leq10^7$ (Ref. 29)], an intermediate state where both EMF and thermal buoyancy are significant ($10^7<$Ra$\leq10^9$), and a final state where EMF effects are very small (Ra$>10^9$). The EMF dominant regime is characterized by a significant heat transfer enhancement in comparison with the neutral state. This is the result of the enhanced mixing and increased level of the turbulent stress (and consequently of the turbulent kinetic energy). The most significant increase in the ratio between the integral heat transfer with and without EMF, which varies between $3\leq\mathrm{Nu}(F_i^L)/\mathrm{Nu}(0)\leq18$, is obtained in $10^4\leq\mathrm{Ra}\leq10^7$ range, Fig. 12—right. Note that the maximal heat transfer enhancement obtained in rotating turbulent Rayleigh–Bénard convection for a very similar range of working regimes was significantly smaller—about 20%, i.e., $\mathrm{Nu}(\Omega)/\mathrm{Nu}(0)\approx1.2$.[30]

The vertical profiles of the long-time and horizontally averaged temperature for different values of Ra and different intensities of applied EMF (I=0, 1, and 10 A) are shown in Fig. 13. Characteristic regions of the temperature distribution can be distinguished: the well-mixed central core with almost uniform temperature and boundary layers in the proximity of the thermally active horizontal walls with very steep temperature gradients. Compared to the neutral situation, EMF elevates temperature in the core region and generates asymmetrical distribution. The temperature in the core region is almost identical for both values of applied EMF (I=1 and 10 A) for the low Ra (Ra=10^6) case. The differences are in the proximity of walls where stronger EMF generates significant thinning of the thermal boundary layer. With Ra increase, the lower intensity EMF profiles (I=1 A) approach

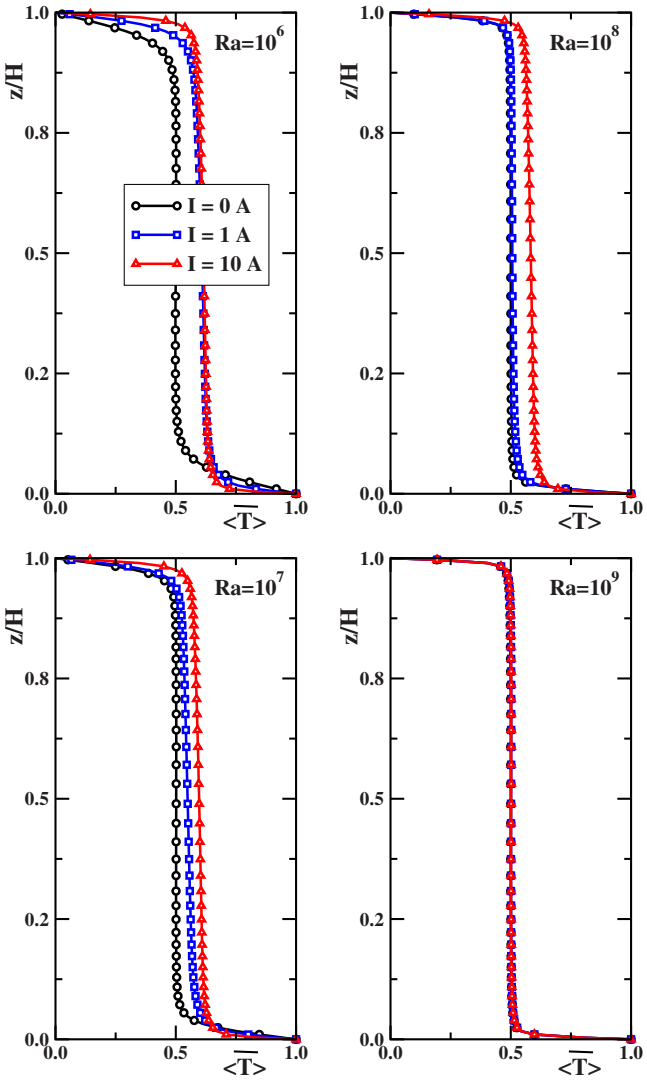

FIG. 13. (Color online) The long-time and horizontally averaged vertical temperature profiles for different values of Ra and different intensities of EMF, I=0, 1, and 10 A.

the neutral situation. In contrast to a uniform magnetic field, a locally applied EMF does not produce temperature inversions in the region that separates boundary layers from the core.[24–26] Finally, for the high Ra case (Ra=10^9), the thermal buoyancy starts to be the most dominant driving mechanism of the flow and EMF does not bring any significant changes in temperature distributions.

To obtain insights into the dynamics of the thermal field under the influence of the EMF, histograms of probability density functions (PDFs) of temperature at two characteristic locations, inside the thermal boundary layer (MON1) and in proximity of the enclosure center (MON2), are shown in Fig. 14. The strong asymmetrical distribution with a characteristic peak at $(T-\bar{T})/\sigma_\theta=-0.5$ is typical for the neutral case and is in excellent agreement with DNS results and experiments shown in Verdoold *et al.*,[28] Fig. 12—top. The positive values indicate ejections of thermal plumes from the boundary layer toward the center of enclosure. Due to EMF action and generated vortical structures, these ejections are significantly intensified—as indicated in a shift toward positive

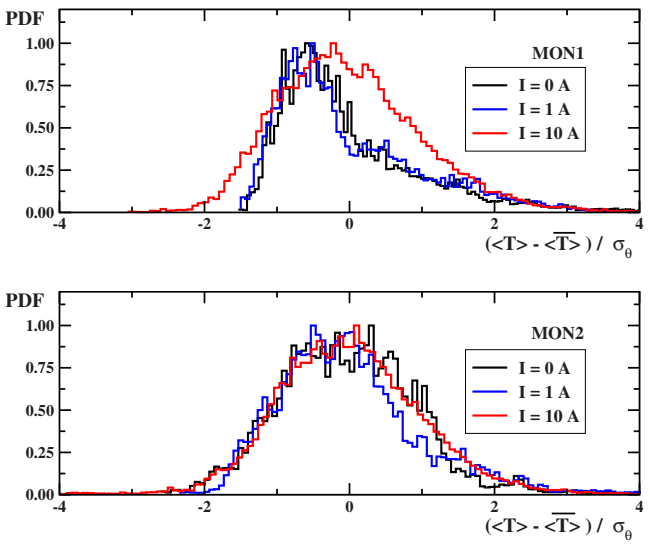

FIG. 14. (Color online) Probability density functions for temperature inside the boundary layer (top) and in the center of the enclosure (bottom), Ra $=10^8$, I=0,1,10 A.

values (I=10 A) shown in Fig. 14—top. For the central location, an interesting nonmonotonic behavior in the PDF distribution is observed, Fig. 14—bottom. The weak EMF (I =1 A) case indicates increased deviation from a symmetrical Gaussian distribution that is recovered for strong EMF (I=10 A). The strong EMF resulted in PDFs that are less skewed at both locations, indicating better mixing. This can be used as an additional proof that anisotropy of the thermal turbulence (associated with fluctuations of thermal field) is also reduced.

IV. CONCLUSIONS

We have shown that application of the locally imposed EMF can be an efficient method in enhancing turbulent mixing and can lead to impressive wall-heat transfer in a generic setup of thermal buoyancy driven turbulent flow. In contrast to the generally accepted view that an imposed magnetic field will suppress velocity fluctuations of an electrically conductive fluid, and in turn will increase the anisotropy of the turbulence, we demonstrated that locally applied EMF can enhance turbulence and make redistribution of the energy among fluctuating velocity components more isotropic compared to its neutral state.

ACKNOWLEDGMENTS

Mr. J. Verdoold is acknowledged for providing photos of the experimental study shown in Fig. 1—middle. The high-performance supercomputing facilities were provided by the NWO/NCF and SARA Computational and Network Services, Amsterdam, The Netherlands.

[1] G. Rüdiger and R. Hollerbach, *The Magnetic Universe: Geophysical and Astrophysical Dynamo Theory* (Wiley, Weinheim, 2004).
[2] E. A. Spiegel, "Cosmic vortices in hot stars and cool disks," Theor. Comput. Fluid Dyn. **24**, 77 (2010).
[3] H. Honji, M. Ohkura, and Y. Ikehata, "Flow patterns of an array of electromagnetically-driven cellular vortices," Exp. Fluids **23**, 141 (1997).

[4]L. Rossi, J. C. Vassilicos, and Y. Hardalupas, "Multiscale laminar flows with turbulentlike properties," Phys. Rev. Lett. **97**, 144501 (2006).
[5]L. Rossi, J. C. Vassilicos, and Y. Hardalupas, "Electromagnetically controlled multi-scale flows," J. Fluid Mech. **558**, 207 (2006).
[6]L. Rossi, S. Bocquet, S. Ferrari, J. M. G. de la Cruz, and S. Lardeau, "Control of flow geometry using electromagnetic body forcing," Int. J. Heat Fluid Flow **30**, 505 (2009).
[7]A. R. Cieślik, L. P. J. Kamp, H. J. H. Clerx, and G. J. F. van Heijst, "Meandering streams in a shallow fluid layer," Europhys. Lett. **85**, 54001 (2009).
[8]Y. Shimomura, "Large eddy simulation of magnetohydrodynamics turbulent channel flows under a uniform magnetic field," Phys. Fluids **3**, 3098 (1991).
[9]G. Akoun and J. P. Yonnet, "3D analytical calculation of the forces exerted between 2 cuboidal magnets," IEEE Trans. Magn. **20**, 1962 (1984).
[10]T. W. Berger, J. Kim, C. Lee, and J. Lim, "Turbulent boundary layer control utilizing the Lorentz force," Phys. Fluids **12**, 631 (2000).
[11]S. Lardeau, S. Ferrari, and L. Rossi, "Three-dimensional numerical simulation of electromagnetically driven multiscale shallow layer flows: Numerical modeling and physical properties," Phys. Fluids **20**, 127101 (2008).
[12]S. Kenjereš, J. Verdoold, M. J. Tummers, K. Hanjalić, and C. R. Kleijn, "Numerical and experimental study of electromagnetically driven vortical flows," Int. J. Heat Fluid Flow **30**, 494 (2009).
[13]S. Kenjereš and K. Hanjalić, "Numerical simulation of a turbulent magnetic dynamo," Phys. Rev. Lett. **98**, 104501 (2007).
[14]S. Kenjereš and K. Hanjalić, "Numerical insights into magnetic dynamo action in a turbulent regime," New J. Phys. **9**, 306 (2007).
[15]S. Kenjereš, "Large eddy simulations of targeted electromagnetic control of buoyancy-driven turbulent flow in a slender enclosure," Theor. Comput. Fluid Dyn. **23**, 471 (2009).
[16]J. Verdoold, "Long-term unsteadiness and large-scale structures in Rayleigh-Bénard convection with and without electromagnetic forcing," Ph.D. thesis, Delft University of Technology, 2010.
[17]S. Kenjereš and K. Hanjalić, "Numerical insights into flow structure in ultraturbulent thermal convection," Phys. Rev. E **66**, 036307 (2002).
[18]S. Kenjereš and K. Hanjalić, "LES, T-RANS and hybrid simulations of thermal convection at high Ra numbers," Int. J. Heat Fluid Flow **27**, 800 (2006).
[19]J. Verdoold, M. J. Tummers, and K. Hanjalić, "Oscillating large-scale circulation in turbulent Rayleigh-Bénard convection," Phys. Rev. E **73**, 056304 (2006).
[20]J. L. Lumley, "Computational modelling of turbulent flows," Adv. Appl. Mech. **18**, 123 (1978).
[21]T. J. Craft, N. Z. Ince, and B. E. Launder, "Recent developments in second-moment closure for buoyancy-affected flows," Dyn. Atmos. Oceans **23**, 99 (1996).
[22]A. Alemany, R. Moreau, P. L. Sulem, and U. Frisch, "Influence of an external magnetic field on homogeneous MHD turbulence," J. Mec. **18**, 277 (1979).
[23]J. Sommeria and R. Moreau, "Why, how and when, MHD turbulence becomes two-dimensional," J. Fluid Mech. **118**, 507 (1982).
[24]S. Cioni, S. Chamumat, and J. Sommeria, "Effect of a vertical magnetic field on turbulent Rayleigh-Bénard convection," Phys. Rev. E **62**, 4520 (2000).
[25]K. Hanjalić and S. Kenjereš, "Reorganization of turbulence structure in magnetic Rayleigh-Bénard convection: A T-RANS study," J. Turbul. **1**, 1 (2000).
[26]K. Hanjalić and S. Kenjereš, "T-RANS simulation of deterministic eddy structure in flows driven by thermal buoyancy and Lorentz force," Flow, Turbul. Combust. **66**, 427 (2001).
[27]S. Kenjereš and K. Hanjalić, "Numerical simulation of magnetic control of heat transfer in thermal convection," Int. J. Heat Fluid Flow **25**, 559 (2004).
[28]J. Verdoold, M. van Reeuwijk, M. J. Tummers, H. J. J. Jonker, and K. Hanjalić, "Spectral analysis of boundary layers in Rayleigh-Bénard convection," Phys. Rev. E **77**, 016303 (2008).
[29]S. Kenjereš, "Electromagnetic enhancement of turbulent heat transfer," Phys. Rev. E **78**, 066309 (2008).
[30]J. Q. Zhong, R. J. A. M. Stevens, H. J. H. Clerx, R. Verzicco, D. Lohse, and G. Ahlers, "Prandtl-, Rayleigh-, and Rossby-number dependence of heat transfer in turbulent rotating Rayleigh-Bénard convection," Phys. Rev. Lett. **102**, 044502 (2009).